Estimation of Shortwave Direct Radiative Forcing of Biomass-Burning Aerosols Using New Angular Models

XIANG LI, SUNDAR A. CHRISTOPHER, JOYCE CHOU, AND RONALD M. WELCH

Department of Atmospheric Sciences, University of Alabama in Huntsville, Huntsville, Alabama

(Manuscript received 7 October 1999, in final form 20 March 2000)

ABSTRACT

Using a new angular distribution model (ADM) for smoke aerosols, the instantaneous top-of-atmosphere (TOA) shortwave aerosol radiative forcing (SWARF) is calculated for selected days over biomass-burning regions in South America. The visible and infrared scanner data are used to detect smoke aerosols and the Clouds and the Earth's Radiant Energy System (CERES) scanner data from the Tropical Rainfall Measuring Mission are used to obtain the broadband radiances. First, the ADM for smoke aerosols is calculated over land surfaces using a discrete-ordinate radiative transfer model. The instantaneous TOA shortwave (SW) fluxes are estimated using the new smoke ADM and are compared with the SW fluxes from the CERES product. The rms error between the CERES SW fluxes and fluxes using the smoke ADM is 13 W m^{-2}. The TOA SWARFs per unit optical thickness for the six surface types range from -29 to -57 W m^{-2}, showing that smoke aerosols have a distinct cooling effect. The new smoke ADM developed as part of this study could be used to estimate radiative impact of biomass-burning aerosols.

1. Introduction

Biomass burning is considered to be one of the major sources of trace gas species and tropospheric aerosol particles (Crutzen et al. 1979). These aerosols play a significant role in atmospheric chemistry (Andreae 1991), earth radiation budget (Penner et al. 1992; Hobbs et al. 1997), and climate (Houghton et al. 1996). Widely prevalent in the Tropics, anthropogenic biomass burning has expanded drastically in the last 15 years because of increased deforestation practices in Brazil's Amazon basin and land clearing for shifting cultivation in South America, Southeast Asia, and Africa (Sailer and Crutzen 1980). It is estimated that 114 Tg of smoke is released into the atmosphere yearly through biomass burning, of which 80% is in the tropical regions (Penner et al. 1992; Hao and Liu 1994).

Smoke aerosols from biomass burning can significantly modify the earth's radiation budget (Penner et al. 1992; Hobbs et al. 1997; Christopher et al. 1996). Smoke aerosols, mainly composed of organic matter and black carbon (Martins et al. 1998), reflect and absorb the solar radiation and therefore have a direct radiative effect. They also serve as cloud condensation nuclei and have an indirect radiative effect by modulating the cloud properties. The direct smoke shortwave (SW) aerosol radiative forcing (SWARF) at the top of atmosphere (TOA), defined as the difference of TOA SW fluxes between clear-sky and smoke conditions, is a measure of direct aerosol SW radiative impact from biomass-burning events. If TOA SW flux over a smoke-aerosol region is larger than that over clear-sky conditions the TOA SWARF is negative. As a result, if SWARF is negative, it implies that more solar radiation is reflected back to space in smoke conditions, and therefore it is called a ''cooling effect.'' Important parameters include the rate of biomass burning, the lifetime of smoke, the fraction of burned material that goes into smoke, the surface albedo, the fractional cloud cover, the fraction of smoke that is distributed between land and ocean, and the optical properties of aerosols that include single-scattering albedo, optical depth, and extinction coefficients. Using these parameters, the direct TOA SWARF of smoke aerosols can be estimated using a simple radiative transfer equation (Penner et al. 1992; Hobbs et al. 1997). However, because of the uncertainty in smoke aerosol characteristics, the estimate of direct TOA SWARF for smoke aerosols is uncertain. The estimated global-mean values of TOA SWARF from biomass-burning aerosols are -0.8 W m^{-2} (Penner et al. 1992) and -0.3 W m^{-2} (Hobbs et al. 1997), respectively. The TOA SWARF difference between the Penner et al. (1992) and Hobbs et al. (1997) estimates is the result of assuming different values of the scattering and absorption efficiencies and the humidification factor of biomass-burning aerosols.

Corresponding author address: Xiang Li, Dept. of Atmospheric Sciences, University of Alabama in Huntsville, Huntsville, AL 35899. E-mail: xli@itsc.uah.edu

Satellite measurements provide a more straightforward approach of estimating regional and global TOA SWARF values for smoke aerosols. Using the combination of Advanced Very High Resolution Radiometer (AVHRR) and Earth Radiation Budget Experiment (ERBE; Barkstrom 1984) measurements, the instantaneous direct TOA SWARFs for smoke aerosols were estimated over South America by Christopher et al. (1996, 1998). More recently, this approach has been extended using Tropical Rainfall Measuring Mission (TRMM) datasets (Christopher et al. 2000, hereinafter CCZLW). Depending upon aerosol concentrations, the instantaneous SWARF can be as high as -70 W m^{-2}.

Measurements from the ERBE instruments aboard the National Oceanic and Atmospheric Administration's polar-orbiting satellites and the Earth Radiation Budget Satellite provided important datasets for the understanding of the Earth radiation budget. This effort of measuring TOA radiative fluxes continues through the subsequent Clouds and the Earth's Radiant Energy System (CERES) instruments aboard the TRMM platform and the upcoming Earth Observing System satellites. In both the ERBE and the CERES scanner products, broadband SW (0.2–5.0 μm) and longwave (LW; 5.0–50 μm) radiances were measured by the scanners. The measured radiances were converted to SW and LW fluxes using the angular distribution model (ADM), which relates the TOA radiances at a specific solar and observing geometry to the TOA fluxes under various surface and atmospheric conditions. There are a total of 12 ERBE ADMs, derived by combining five surface types (ocean, land, snow, desert, mixed, or, coastal) with four cloud conditions (clear, partly cloudy, mostly cloudy, and overcast; Green 1987). Although the TOA radiances were accurately measured with careful calibration procedures, the accuracy of ERBE TOA fluxes was affected by the accuracy of ERBE ADMs, as well as by the scene identification, which determines the proper ERBE ADM to be used. Suttles et al. (1992) showed that the estimated SW albedo systematically increases with increasing viewing zenith angle and LW fluxes decrease with increasing viewing zenith angle, because of limitations in the ERBE ADM. The limited number of ERBE ADMs also limits the accuracy of converted ERBE fluxes. To overcome these problems, the CERES team is developing a new generation of CERES ADMs (Green et al. 1995). It is expected that increased accuracy of CERES cloud-property determination and the new ADMs can reduce the uncertainty in the flux conversion by a factor of 3 to 4 (Wielicki et al. 1995). However, note that in both the ERBE and the CERES projects the ADM for smoke is not available. Lacking proper scene categories, smoke aerosols are usually classified as either clear or partly cloudy in the ERBE and CERES products. Because of strong absorption of smoke aerosols on solar radiation and differences in particle size distributions between clouds and smoke, the ADMs for clouds and smoke could be significantly different. This may cause uncertainties in the estimation of TOA SW fluxes over biomass-burning regions in the ERBE and the CERES products. Therefore, an ADM for smoke aerosols will improve the accuracy of CERES SW fluxes over biomass-burning regions.

In this paper, we calculate an ADM for smoke aerosols and examine the ADM effect on the TOA SW fluxes over biomass-burning regions in the CERES product. First, a plane-parallel discrete-ordinate radiative transfer model is used to calculate the smoke ADM using optical properties of smoke aerosols obtained from the Smoke, Cloud, and Radiation—Brazil (SCAR-B) experiment (Kaufman et al. 1998). The calculated smoke ADM is a function of aerosol optical properties, surface albedo, and solar and satellite viewing geometry. Using the visible and infrared scanner (VIRS) imagery, smoke pixels are detected, and the optical thickness of the detected smoke pixels is retrieved. The TOA SW fluxes for smoke aerosols are obtained using the measured CERES radiances and the calculated ADMs for smoke aerosols. Then, we compare the calculated TOA SW fluxes for smoke aerosols with those obtained from the CERES ERBE-Like Instantaneous TOA Estimates (ES-8) data product. Last, we estimate the instantaneous TOA SWARF over smoke regions based on the local ecosystems and compare the differences of the TOA SWARFs computed using the calculated TOA SW fluxes and using the CERES ES-8 ERBE-like data product. This attempt is one of the first to estimate the uncertainty of instantaneous smoke TOA SWARF caused by the uncertainty in angular distribution models.

In section 2, the VIRS and the CERES data products used in this study are introduced. Section 3 presents the calculation of smoke ADMs using the radiative transfer model and then compares the calculated ADM for smoke aerosols with some of the ERBE ADMs. The sensitivity of the calculated ADMs to aerosol optical properties and surface albedos is examined. Results and analyses are shown in section 4. The instantaneous TOA SWARFs of smoke aerosols are estimated, and comparisons are made for smoke TOA SWARFs between use of the calculated ADM and the CERES data product. Section 5 concludes the paper.

2. Satellite data and study area

TRMM provides detailed and comprehensive datasets for the studies of the distribution of rainfall and latent heating, as well as the atmosphere's radiation budget in the Tropics. Two TRMM datasets are used in this study: 1) VIRS Level 1B, and 2) CERES ES-8 ERBE-like product. We focus on the 1998 burning season over land in South America in August 1998. The area of study is between 35°S and 5°N and between 80° and 40°W.

a. VIRS Level-1B data

VIRS measures reflected solar and emitted terrestrial radiation in five spectral channels. The central wave-

lengths of the five channels are 0.63, 1.61, 3.75, 10.8, and 12.0 μm, respectively, with a spatial resolution of 2.11 km at nadir (Kummerow et al. 1998). In this study, version 4 of the VIRS Level-1B data product is used. The Level-1B dataset contains calibrated radiances measured from the five channels of the instrument. The channel-1 and -2 radiances are converted to reflectances, and the channel-3, -4, and -5 radiances are converted to brightness temperatures. Because the measured radiances in the 3.75-μm channel contain contributions from both solar and thermal components, a sixth channel (channel-3 reflectance) is created by removing the thermal emission part using the 10.8-μm channel information (Kaufman and Nakajima 1993). The VIRS radiometer is calibrated using ground testing and in-flight data. In-flight calibration of channels 1 and 2 is accomplished via an onboard solar diffuser and by using the moon as a calibration source (Keiffer and Wildey 1996), and calibration of channels 3, 4, and 5 is accomplished via an onboard blackbody and a space view (Kummerow et al. 1998).

b. CERES ES-8 ERBE-like data

The CERES scanner on the TRMM platform is a broadband instrument (Wielicki et al. 1996) that measures the total (0.3–50 μm), SW (0.3–5.0 μm), and LW (5.0–50.0 μm) radiances. The measured radiances are converted to fluxes using ADMs (Suttles et al. 1988, 1989) developed as part of the ERBE project and are called the CERES ES-8 ERBE-like product. In this study, the Level-2 CERES ES-8 ERBE-like dataset is used. The CERES scanner has two scanning modes: the normal cross-track scanning mode and the rotational scanning mode. In this study, only CERES ES-8 ERBE-like data from the cross-track scanning mode are used.

c. Collocation of VIRS and CERES

The VIRS data product includes measurements at five narrow spectral channels with a spatial resolution of about 2 km at nadir. It can be used to identify smoke pixels and to retrieve optical properties of smoke aerosols (CCZLW). On the other hand, the CERES data product provides TOA radiative fluxes at a reduced spatial resolution. Collocating the two data products is necessary to establish the relation between aerosol optical properties and the TOA SWARF for smoke aerosols. For a VIRS pixel and a CERES footprint to be considered collocated, the geographical difference between the VIRS pixel and the center of the CERES footprint must be less than 0.02°. Both the spatial resolution of a CERES footprint and the spatial resolution of a VIRS pixel change with scanning angle. For example, at nadir, the spatial resolution of a CERES footprint is 8 km in the across-track and 16 km in the alongtrack direction; at a scan angle of 63° toward the edge of the swath, the spatial resolutions increase to 116 km and 16 km in the across and along directions, respectively (Green and Wielicki 1995). The collocation procedure accounts for the change of the CERES and VIRS pixel sizes with scanning angle.

3. Angular distribution model for smoke aerosols

The measured radiance from the CERES scanner at specific sun–satellite angle is converted to TOA flux (Green et al. 1995) using the following equation:

$$F^{\uparrow}_{\mathrm{TOA}} = \frac{\pi I(\theta_0,\ \theta,\ \varphi)}{\xi(\theta_0,\ \theta,\ \varphi)}, \tag{1}$$

where $I(\theta_0, \theta, \varphi)$ is the sensor-measured radiance at solar zenith angle θ_0, satellite zenith angle θ, and relative azimuth angle between the sun and satellite φ; $\xi(\theta_0, \theta, \varphi)$ is the ADM value that relates radiance to flux at a specific solar and satellite viewing geometry; and $F^{\uparrow}_{\mathrm{TOA}}$ is the TOA upward flux at 0.3–5.0 μm for the SW channel. As a result, the accuracy of converted TOA SW fluxes over biomass-burning regions depends upon the accuracy of the ADMs for smoke aerosols.

The Santa Barbara Discrete-Ordinate Atmospheric Radiative Transfer Model SBDART; Ricchiazzi et al. (1998), is used to calculate the shortwave (0.28–4.0 μm) ADMs for horizontally homogeneous smoke aerosols over different surface types. SBDART is a detailed plane-parallel radiative transfer code based on the discrete-ordinate approach (Stamnes et al. 1988). The radiative processes included in the model are Rayleigh scattering, gaseous absorptions, cloud and aerosol scattering, and absorptions. Gaseous absorptions are considered in the model based on the low-resolution band models developed for the LOWTRAN-7 (low-resolution transmittance model) atmospheric transmission code (Pierluissi and Peng 1985). To use gas transmission functions in discrete-ordinate radiative transfer, the band models are approximated with a three-term exponential fit (Wiscombe and Evans 1977). The SBDART model can compute the radiative effects of several common boundary layer and upper-level atmosphere aerosol types, including rural, urban, or maritime aerosols in the boundary layer, as well as fresh and aged volcanic aerosols in the upper atmosphere. User-defined aerosol types are allowed in the SBDART model, which is characterized by the spectral aerosol extinction coefficient (σ_e), aerosol single-scattering albedo (ω_0), and asymmetry factor g.

The spectral optical properties of smoke aerosols used in this study are obtained from the SCAR-B experiment. The smoke particles are modeled as organic liquid shells with black carbon cores (Ross et al. 1998). The volume size distribution of smoke aerosols is assumed to be lognormal with a mode radius of 0.15 μm (Remer et al. 1998). Smoke particles are assumed to be spheres, which is well supported by SCAR-B measurements (Martins et al. 1998), and Mie theory applied to stratified spheres (Ackerman and Toon 1981) is used to calculate

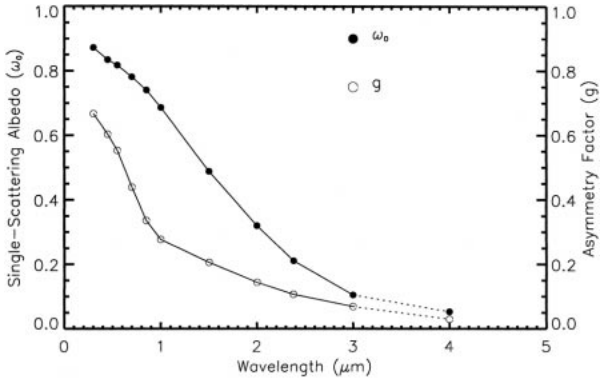

FIG. 1. Smoke single-scattering albedo ω_0 and asymmetry factor g as a function of wavelength used in this study.

the light scattering and absorption coefficients of the smoke aerosols. Figure 1 shows the single-scattering albedo and asymmetry factor as a function of wavelength. The curves at 3.0–4.0 μm are extrapolated from the curves at 0.30–3.0 μm because Ross et al. (1998) provide values only up to 3.0 μm.

In the smoke ADM calculations, a standard tropical atmosphere (McClatchey et al. 1972) is assumed. The surface is assumed to be Lambertian; the uncertainty of this assumption is discussed later in this section. In this study, we refer to the calculated ADM for smoke aerosols as *smoke ADM*. The smoke ADM is a function of aerosol optical thickness τ, ω_0, broadband surface albedo α_s, θ_0, θ, and φ. The τ and ω_0 values are specified at 0.64 μm unless stated otherwise. The aerosol values of τ are calculated in the range from 0.36 to 3.6 in steps of 0.36. The four ω_0 values are 0.70, 0.79, 0.82, and 0.85, respectively; that is well within the range of measurements (Reid et al. 1998). There are 10 solar zenith angles, with cosine of the angles decreasing from 0.90 to 0.45 in steps of 0.05. There are 15 satellite zenith angles, with cosines of the angles decreasing from 1.0 to 0.3 in steps of 0.05. Values of φ range from 0° to 180°, with intervals of 22.5°. There are four values of α_s: 0.10, 0.15, 0.20, and 0.25, covering the range for the surface types in biomass-burning regions.

Figures 2a–d show the calculated ADMs for aerosol values of τ of 0.36, 1.1, 1.8, and 2.5, respectively. The aerosol ω_0 value is assumed to be 0.85, that is, the average value of regionally aged aerosols (Reid et al. 1998); α_s is assumed to be 0.15; and solar zenith angle is assumed to be 36.9°. The relative azimuth angle of 0° represents the forward direction of scattering. From Figs. 2a–d, the ADM value increases with increasing satellite zenith angle. When the τ value is 0.36, the ADM values in the forward-scattering direction (φ = 0°) increase from 0.87 to 1.34, and values in the backward-scattering direction (φ = 180°) increase from 0.87 to 1.11 as θ values increase from 0° to 69.5°. When the τ value increases from 0.36 to 2.5, the ADM values in the forward direction increase from 0.83 to 1.49, and values in the backward direction increase from 0.83 to 0.96 as θ values increase from 0° to 69.5°. The range of ADM values in the forward direction increases and values in the backward direction decrease with increasing value of τ. Comparison of Figs. 2c and 2d shows no important difference between the two ADMs, indicating that the smoke ADM is not sensitive to the value of τ when τ is larger than 1.8 (heavy smoke concentration). Figures 2e and 2f show smoke ADMs with the same ω_0 and solar zenith angle as in Figs. 2a and 2c, but with the value of α_s increased from 0.15 to 0.20. The τ values for Figs. 2e and 2f are 0.36 and 1.8, respectively. Comparison of Figs. 2f and 2c, with τ = 1.8, shows no large difference between the two ADMs, indicating that when aerosol τ is large the smoke ADM is less dependent on the surface albedo (surface type). Comparison of Figs. 2e and 2a, with τ = 0.36, shows large differences in the smoke ADMs. In the forward- and backward-scattering directions, the ADM values in Fig. 2e range from 0.91 to 1.28 and from 0.91 to 1.07, respectively. In comparison with Fig. 2a, the range of ADM values decreases in both the forward- and backward-scattering directions because, for small aerosol τ value, the surface albedo has a greater impact on the smoke ADM. Figures 2g and 2h show the smoke ADMs with the same τ, ω_0, and α_s values as in Figs. 2e and 2f, correspondingly, but with solar zenith angle increased from 36.9° to 60°. In Fig. 2h, the ADM values range from 0.73 to 2.12 and from 0.73 to 0.90, respectively, in the forward- and backward-scattering directions as θ values increase from 0° to 69.5°. Comparison of Figs. 2f and 2h shows that the range of smoke ADM values in the forward-scattering direction greatly increases with increasing solar zenith angle. With larger solar zenith angle, the smoke ADM is less isotropic.

Because most of the smoke-occupied CERES footprints are classified as either clear or partly cloudy in the ES-8 ERBE-like data product, we compare the smoke ADMs with two ERBE ADMs: clear over land as shown in Fig. 2i, and partly cloudy over land as shown in Fig. 2j, for solar zenith angle of 60°. Although the ranges of ADM values are similar between smoke ADMs and ERBE ADMs, the patterns of the two types of ADMs are different. The ERBE ADMs are more sensitive to azimuth angle. The ERBE clear ADM (Fig. 2i) has larger ranges of values in the forward- and backward-scattering angles than that for smoke ADM at τ value of 0.36. Comparison of Figs. 2h and 2j shows that the range of smoke ADM values is larger than that of the ERBE ADM in the forward-scattering direction and is smaller than that of the ERBE ADM in the backward-scattering direction. The mean absolute difference between the ADMs in Figs. 2g and 2i is 0.102, and the relative difference is 10.3%. The mean absolute difference between the ADMs in Figs. 2h and 2j is 0.101; the relative difference is 9.8%.

Using new ADMs for cloudy conditions, Lubin and Webber (1995) showed that the net surface SW fluxes

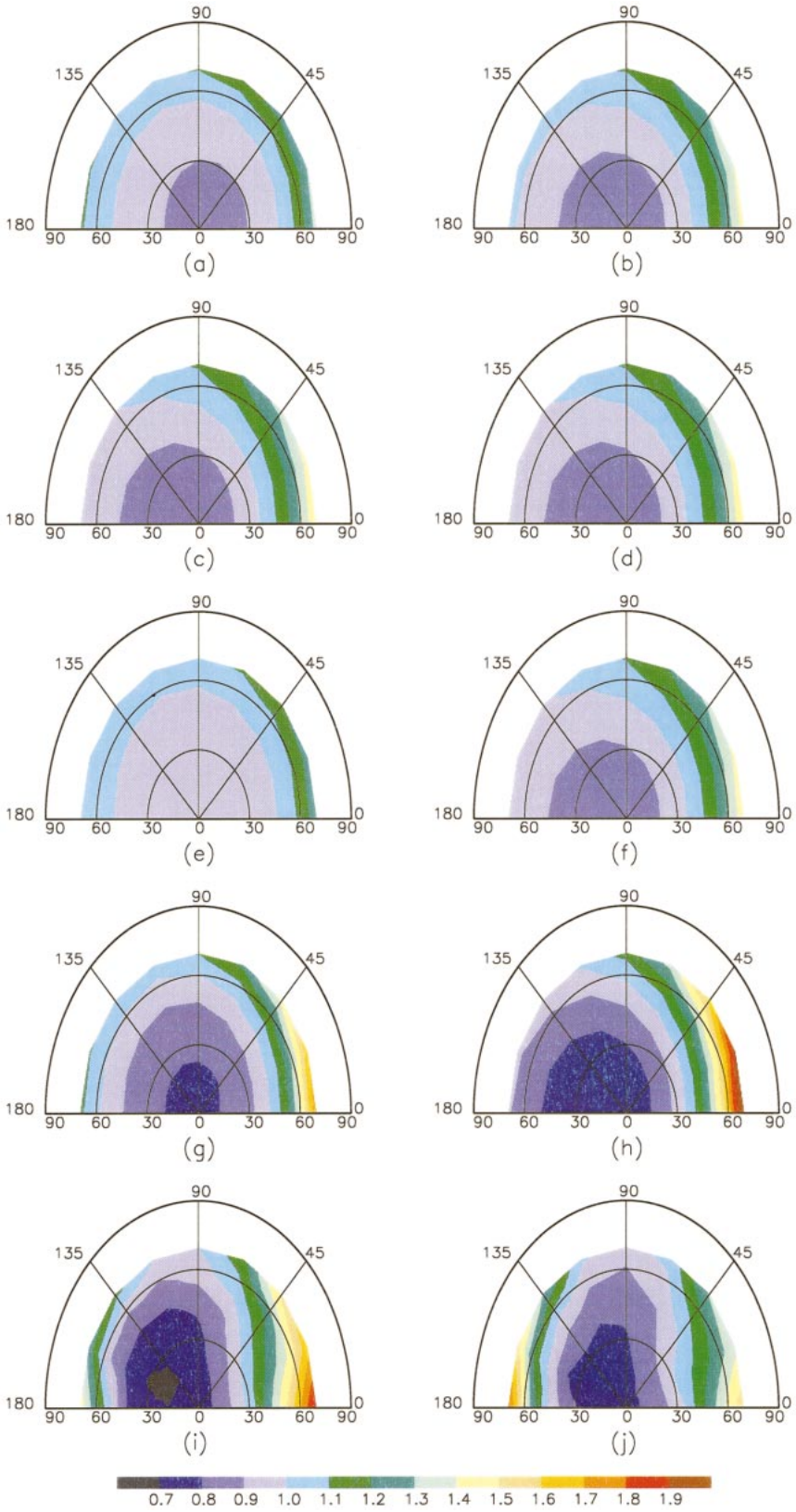

under a cloud condition over the ocean surfaces are different from the ERBE ADMs by 20–60 W m^{-2}. The surface radiative fluxes are often estimated from the TOA radiative fluxes using some established relationships from atmospheric radiative transfer (Li et al. 1993). In biomass-burning regions, a 10% uncertainty in TOA SW fluxes can cause significant errors of surface SW fluxes, because smoke aerosols are normally less reflective than clouds and most of the incoming solar fluxes reach the surface. Therefore, smoke ADMs are necessary to improve the accuracy of estimated SW fluxes, especially at the surface.

Because the smoke ADM is a function of τ, ω_0, and α_s, uncertainties in these values cause uncertainties in the smoke ADM values. Because the TOA clear-sky albedo is directly related to α_s in clear-sky conditions, the sensitivity of smoke ADM to the parameters of τ, ω_0, and TOA clear-sky albedo is examined. Figure 3a shows the ADM value as the function of smoke τ value. The ω_0, TOA clear-sky albedo, and θ values are 0.85, 0.15, and 40°, respectively. The solar zenith angles are assumed to be 30° and 60°, respectively. The relative azimuth angles are assumed to be 45° (forward scattering) and 135° (backward scattering), respectively. From Fig. 3a, it is seen that the ADM values are not sensitive to the values of τ when τ is larger than 1.7. When τ is less than 1.7, the ADM values become more sensitive to the τ values, especially at the larger solar zenith angles. When θ_0 is 60°, the ADM values vary from 0.97 to 1.04 as the τ values vary from 0.35 to 1.5, an increase of about 7%. Figure 3b shows the ADM values as a function of ω_0. In this case, the τ value is 1.1, and TOA clear-sky albedo and solar and satellite viewing geometry are the same as the ones in Fig. 3a. The ADM values are less sensitive to values of ω_0 when the ω_0 value is less than 0.81, becoming more sensitive to ω_0 as the ω_0 values become larger than 0.81. The ADM values vary by less than 3% when the ω_0 value varies from 0.76 to 0.85. Figure 3c shows the ADM values as a function of TOA clear-sky albedo. The ω_0 value is 0.85 and τ value is 1.1. The solar zenith angle, satellite angle, and relative azimuth angle are set to be the same as in Figs. 3a and 3b. From Fig. 3c, it is seen that the ADM values are slightly more sensitive to TOA clear-sky albedo in the backward-scattering direction than in the forward-scattering direction. The ADM value varies from 0.92 to 0.97 as clear-sky albedo changes from 0.10 to 0.24, a change of about 5%. In general, we conclude that the smoke ADMs are relatively insensitive to the smoke optical properties and TOA clear-sky albedos. For most cases, the uncertainty of smoke ADM is expected to be less than 10% because of the uncertainties of these parameters.

The asymmetry factor, mainly determined by the particle size distribution of smoke aerosols, has an effect on the reflected solar radiation at the TOA. As a result, the smoke ADM is affected by the asymmetry factor. Ross et al. (1998) shows that, during SCAR-B, g (0.64 μm) can range from 0.40 to 0.55 for a variety of smoke aerosol size distributions. The uncertainty of smoke ADM caused by the uncertainty of asymmetry factor is examined (Fig. 4a). The ω_0 and α_s values are 0.85, 0.15, respectively. The θ_0, θ, and φ values are 60°, 40°, and 45°, respectively. The sensitivity of ADM values to the asymmetry factor is examined for three τ values: 0.35, 1.06, and 1.78. From Fig. 4a, the uncertainty of smoke ADM values caused by the variation of g values is within 2%. The uncertainty of smoke ADM caused by the assumed constant spectral surface albedo also is examined and is shown in Fig. 4b. The ω_0 value is 0.85. The θ_0 and θ values are 60° and 40°, respectively. The φ values are 45° and 135°, respectively. In Fig. 4b, constant albedo means the ADM values are calculated assuming constant spectral surface albedo with the value of 0.169, and vegetation means the ADM values are calculated using the vegetation spectral surface albedo as specified in SBDART with the equivalent broadband albedo of 0.169. From Fig. 4b, the uncertainty of smoke ADM values caused by the uncertainty of spectral surface albedo decreases with increasing τ for both the forward-scattering direction and the backward-scattering direction. The uncertainty can be as high as 5% when τ is less than 0.8.

The accuracy of smoke ADM is affected by the assumption of Lambertian surface. From the aircraft measurements during SCAR-B, surface reflectance is found to be anisotropic over cerrado and forest (Tsay et al. 1998). Also, the bidirectional reflectance distribution functions (BRDF) for cerrado and forest surfaces are different. The uncertainty of smoke ADM caused by the assumption of Lambertian surface is examined in this study, and results are shown in Fig. 4c. Again, the ω_0 value is assumed to be 0.85. The θ_0 and θ values are 60° and 40°, respectively. The φ values are 45° and 135°, respectively. Cerrado BRDF means that the smoke ADM values are calculated using the BRDF over cerrado as shown in Plate 2 of Tsay et al. (1998). When τ is larger than 0.8, the uncertainty of smoke ADM values is less than 4%. This result is expected, because the smoke-scattering effect dominates over surface reflectance when τ gets large. However, when τ is smaller than 0.5, the uncertainty is significant and can reach

←

FIG. 2. The calculated smoke ADMs with (a) $\tau = 0.36$, $\omega_0 = 0.85$, $\alpha_s = 0.15$, $\theta_0 = 36.9°$; (b) $\tau = 1.10$, $\omega_0 = 0.85$, $\alpha_s = 0.15$, $\theta_0 = 36.9°$; (c) $\tau = 1.80$, $\omega_0 = 0.85$, $\alpha_s = 0.15$, $\theta_0 = 36.9°$; (d) $\tau = 2.5$, $\omega_0 = 0.85$, $\alpha_s = 0.15$, $\theta_0 = 36.9°$; (e) $\tau = 0.36$, $\omega_0 = 0.85$, $\alpha_s = 0.20$, $\theta_0 = 36.9°$; (f) $\tau = 1.8$, $\omega_0 = 0.85$, $\alpha_s = 0.15$, $\theta_0 = 36.9°$; (g) $\tau = 0.36$, $\omega_0 = 0.85$, $\alpha_s = 0.20$, $\theta_0 = 60°$; (h) $\tau = 1.8$, $\omega_0 = 0.85$, $\alpha_s = 0.15$, $\theta_0 = 60°$; (i) the ERBE clear over land ADM; and (j) ERBE partly cloudy over land.

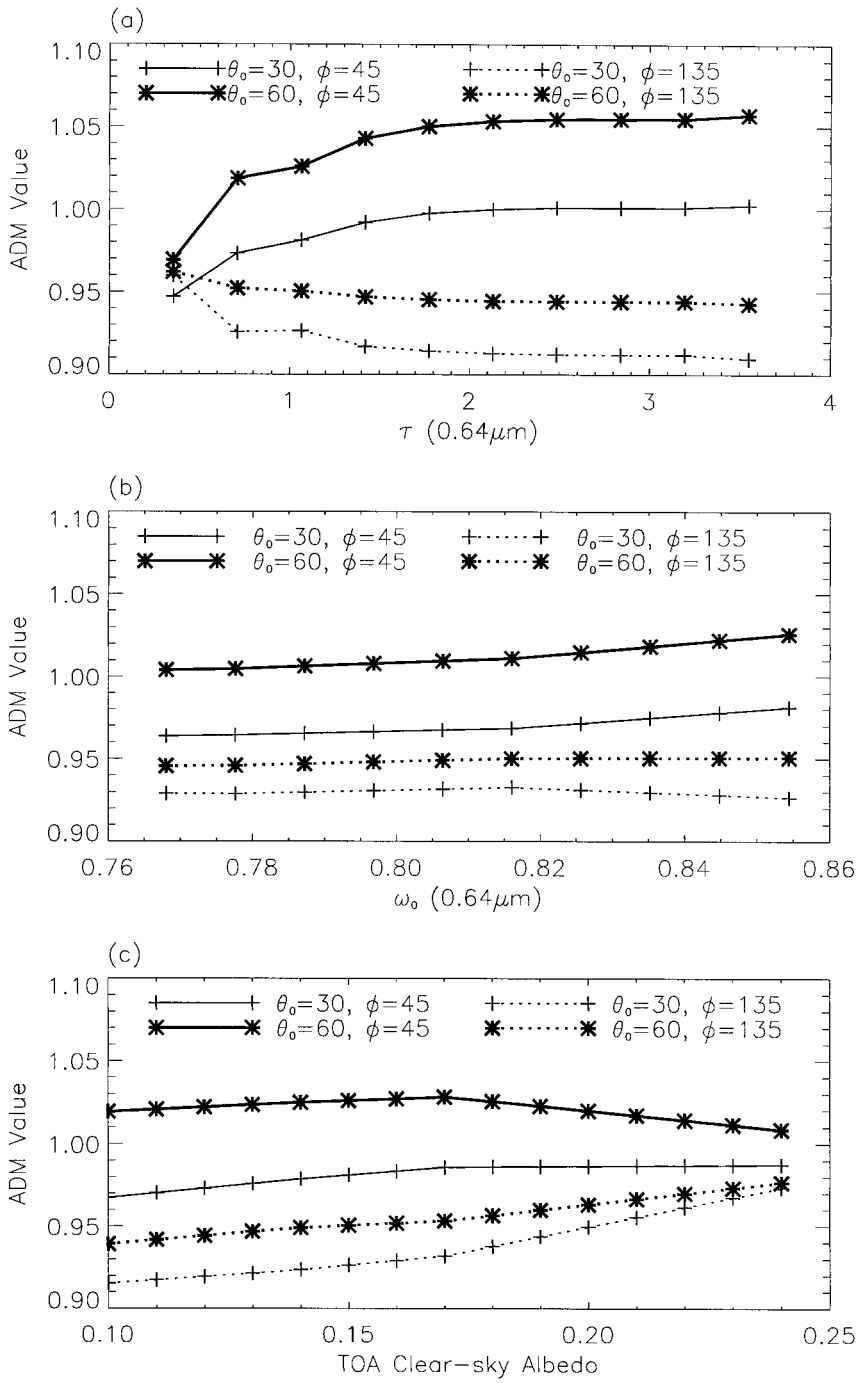

FIG. 3. Sensitivity of smoke ADM as function of (a) τ, (b) ω_0, and (c) TOA clear-sky albedo.

about 10%, suggesting that BRDF is necessary to obtain accurate smoke ADM values with light smoke loading.

4. Results and discussion

The VIRS Level-1B data and the CERES ES-8 ERBE-like data in August 1998 are used to analyze instantaneous smoke TOA SWARF over South America. Table 1 lists the information of the 14 VIRS data files used in this study, including the observing date, time, and geographical coverage. Smoke can be seen clearly from the channel-1 images of these VIRS data files. Figure 5a shows an example of the channel-1 image of the VIRS data. In Fig. 5a, the lower part of the image clearly shows high cloud amounts.

A smoke detection algorithm based on simple thresh-

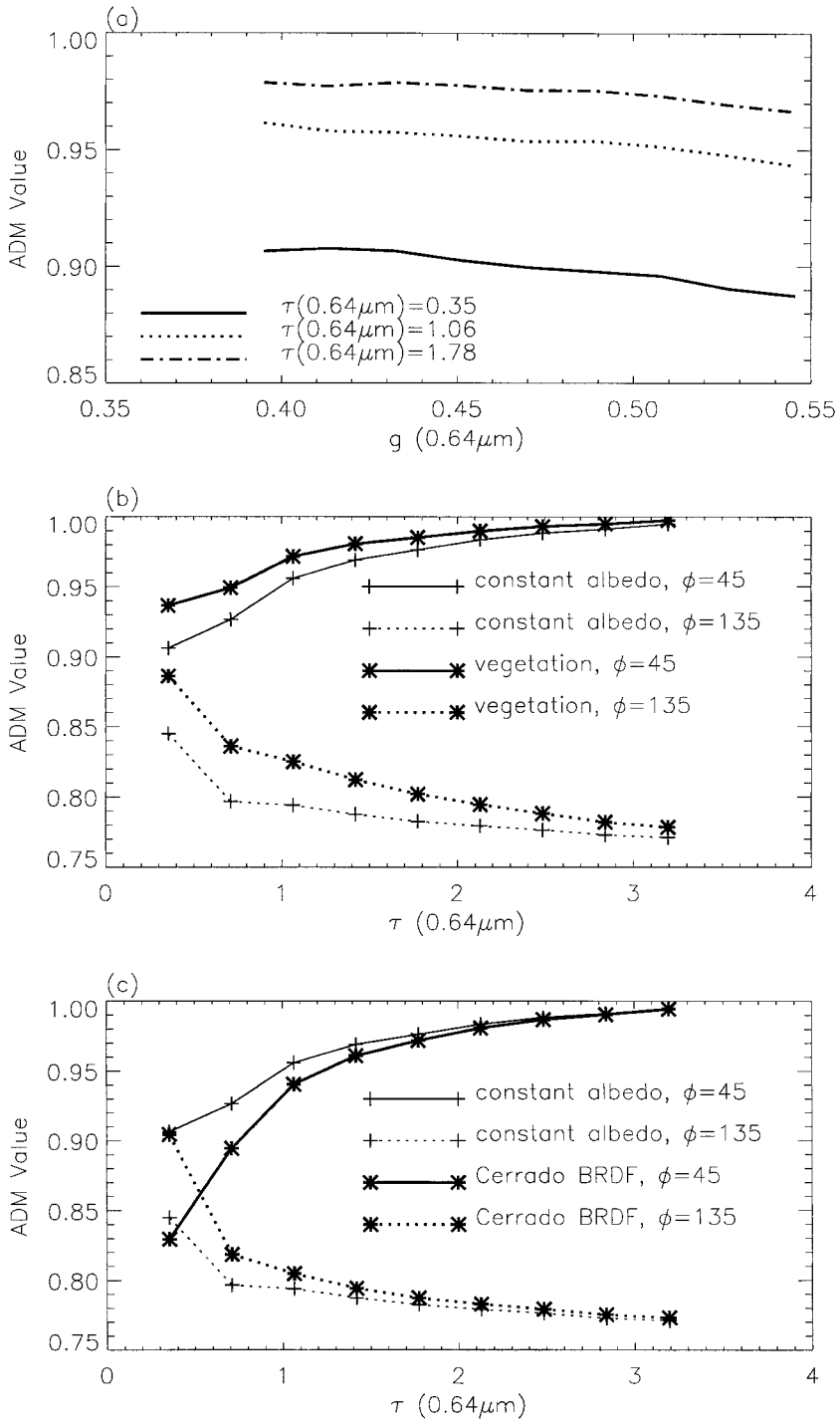

FIG. 4. (a) Sensitivity of smoke ADM as a function of *g*, (b) influence of wavelength-dependent surface albedo on the smoke ADM values, and (c) influence of surface BRDF on the smoke ADM values.

olds is developed in this study. This algorithm identifies smoke pixels from the VIRS images over land surfaces using channel-1 reflectance (R1), channel-2 reflectance (R2), channel-3 reflectance (R3), channel-4 brightness temperature (T4), and channel-5 brightness temperature (T5). A number of thresholds are used to identify a VIRS pixel as a cloud, smoke, or clear-sky pixel (Fig. 6). First, isolated cumulus clouds are identified using a 5×5 window region around a VIRS pixel. If the standard deviation of channel-1 reflectance (σ_{R1}) for the pixels

TABLE 1. A list of VIRS data files used in the smoke detection and smoke SWARF forcing investigation.

No.	Year	Month	Day	Lat (°)		Long (°)		Start time (UTC)	End time (UTC)
				Min	Max	Min	Max		
1	1998	08	11	−23.79	−7.80	−67.26	−47.35	11.9822	12.0668
2	1998	08	11	−13.14	3.55	−50.95	−32.07	12.0669	12.1514
3	1998	08	13	−16.79	−0.23	−59.13	−40.04	11.2190	11.3036
4	1998	08	23	−15.44	1.19	−71.30	−52.31	20.1765	20.2611
5	1998	08	25	−17.38	−0.83	−71.62	−52.49	19.3722	19.4568
6	1998	08	25	−24.03	−11.92	−56.01	−41.83	19.4569	19.5110
7	1998	08	26	−15.44	1.18	−64.10	−45.12	18.1843	18.2689
8	1998	08	27	−15.44	1.18	−53.88	−34.90	17.0093	17.0939
9	1998	08	27	−19.41	−2.99	−71.65	−52.33	18.5624	18.6470
10	1998	08	27	−29.07	−13.88	−55.79	−34.91	18.6470	18.7316
11	1998	08	28	−15.45	1.17	−67.13	−48.13	17.3633	17.4478
12	1998	08	28	−25.80	−10.05	−51.69	−31.46	17.4479	17.5324
13	1998	08	29	−21.54	−5.30	−71.64	−52.06	17.7637	17.8482
14	1998	08	29	−34.38	−20.81	−69.56	−47.26	19.4142	19.4987

in the window is larger than 0.04, the window region is labeled as cloud and no further processing will be done on these pixels. A number of thresholds are sequentially used to identify bright and thick clouds, high and cold cirrus clouds, low clouds, optically thick smoke (R1 is usually over 0.30), dense smoke (R1 is usually over 0.20), optically thin smoke haze (R1 is usually less than 0.20), and clear-sky conditions. The ratio of R2 to R1 is used to separate smoke pixels from clear-sky pixels over land. For the vegetation surface types, surface spectral albedo at 1.6 μm (channel 2) is much higher than that that at 0.64 μm (channel 1). As a result, the values of R2:R1 are usually larger than 2.0. The existence of smoke aerosols increases channel-1 reflectance and the values of R2:R1 decrease. The threshold of 1.9 for R2:R1 is used, which separates most of the clear-sky pixels from smoke pixels for the 14 images that were studied. This smoke detection algorithm works well to identify cloud, smoke, and clear-sky pixels for all the 14 VIRS data files in this study. The accuracy of the detection scheme was tested by visually comparing the results with the visible imagery from VIRS. Figure 5b shows the scene identification image corresponding to the VIRS image in Fig. 5a. The black color represents clear sky over lands. The gray color represents clouds, and the white color represents smoke aerosols. Comparison with Fig. 5a shows that smoke haze, clouds, and clear-sky pixels are properly identified.

For the smoke pixels detected from the VIRS images, aerosol optical thicknesses are retrieved using the VIRS channel-1 images. A table lookup approach, the same as the one used in the retrieval of τ from the AVHRR channel-1 images (Li et al. 1999), is used for the τ retrieval. The SBDART model is used to produce the lookup table. Smoke aerosols are assumed to be spherical with an organic liquid shell and black carbon core. The particle size distribution of smoke aerosols is assumed to be lognormal. Mie theory is used to calculate the spectral optical properties of smoke aerosols, and they match well with the ones obtained from the SCAR-B experiment (Ross et al. 1998). This approach was validated in the satellite retrieval of ω_0 during SCAR-B in the 1995 burning season. The retrieved ω_0 values are in good agreement with the ones obtained from in situ aircraft measurements during SCAR-B. A detailed description of this retrieval approach is given in Li et al. (1999).

The τ values for smoke aerosols are retrieved from the VIRS channel-1 images assuming the aerosol ω_0 values based on the surface types defined in the International Geosphere–Biosphere Programme (IGBP). There are a total of 18 surface types, covering different vegetation surfaces over land, ocean, and ice (Loveland and Belward 1997). The radiative effect of smoke over the surface types of forest, savanna, grassland, wetland, mixed forest, and cropland is examined in this study. The ω_0 values at the wavelength of 0.55 μm for surface types of forest, savanna, grassland, and wetland are assumed to be 0.881, 0.862, 0.924, and 0.892, respectively, which are the mean ω_0 values for the corresponding surface types retrieved from the AVHRR imagery during SCAR-B, and the results agree well with the in situ measurements (Reid et al. 1998). For the other surface types, the ω_0 value of 0.88 at 0.55 μm is assumed, which is in the ω_0 range of 0.8–0.9 as obtained during SCAR-B (Reid et al. 1998).

Surface albedo is a key parameter in both the lookup table for smoke τ retrieval and in the smoke ADMs. Because satellite sensors detect SW radiation at TOA, the clear-sky albedo at TOA can be directly estimated from the satellite observations. In this study, the SBDART model is used to calculate the relation between TOA albedo and surface albedo under clear-sky conditions assuming the standard tropical atmosphere (McClatchey et al. 1972). The result is that the surface albedo can be inferred from the TOA clear-sky albedo.

The VIRS channel-1 TOA clear-sky albedo map is determined as follows. The study area is first divided

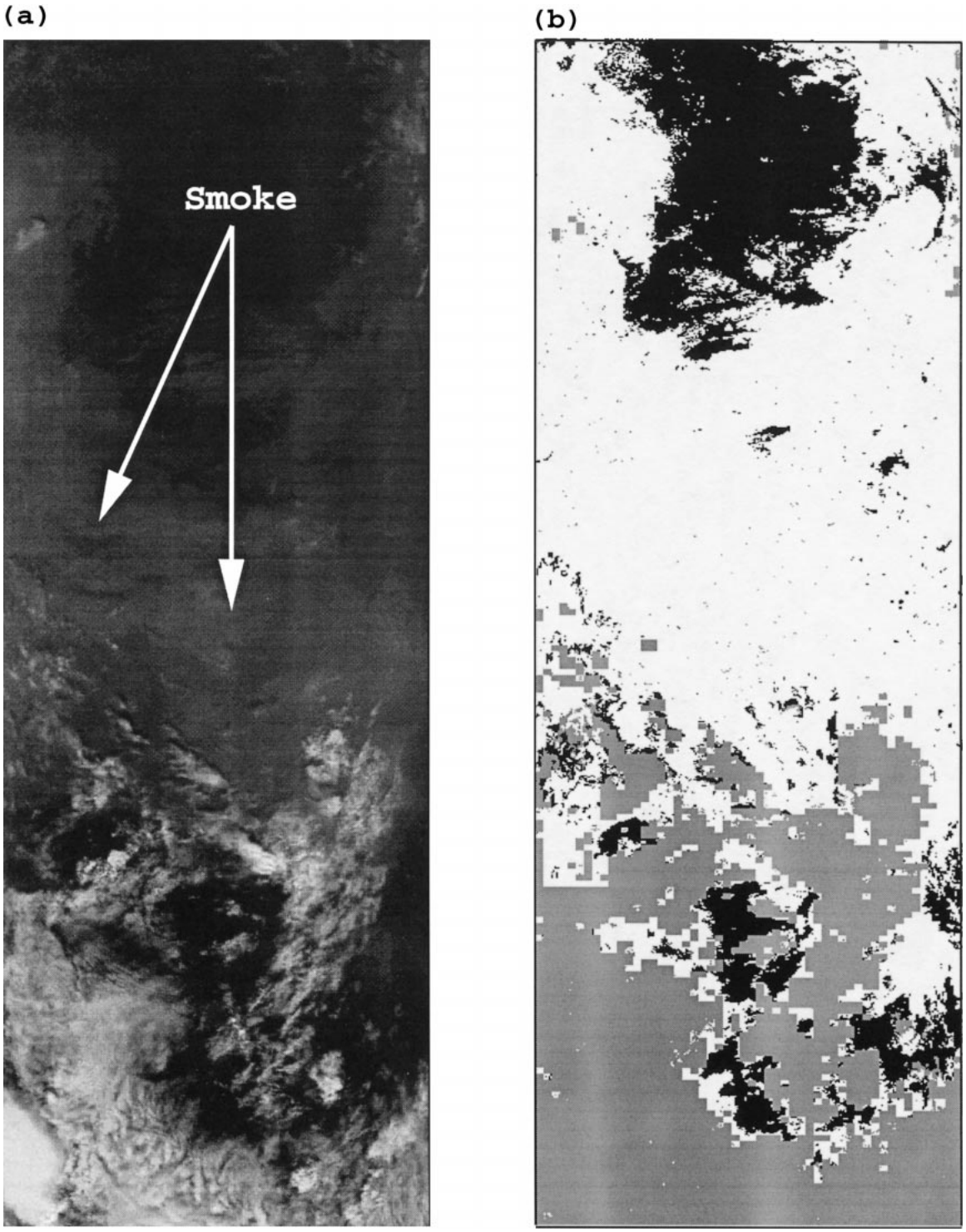

FIG. 5. (a) VIRS channel-1 image for datafile 9, (b) corresponding scene identification, black: clear; gray: cloud; white: smoke.

into 4 km × 4 km grids. The clear-sky albedo is determined by assigning the minimum R1 value obtained from all pixels falling into this grid. All VIRS data files in August 1998 are used to obtain this clear-sky albedo map.

The broadband TOA clear-sky albedo map is determined in three steps. First, the study area is also divided into a 20 km × 20 km grid. If the percentage of clear-sky pixels for a collocated VIRS–CERES sample is greater than 90%, we assume that this collocated sample

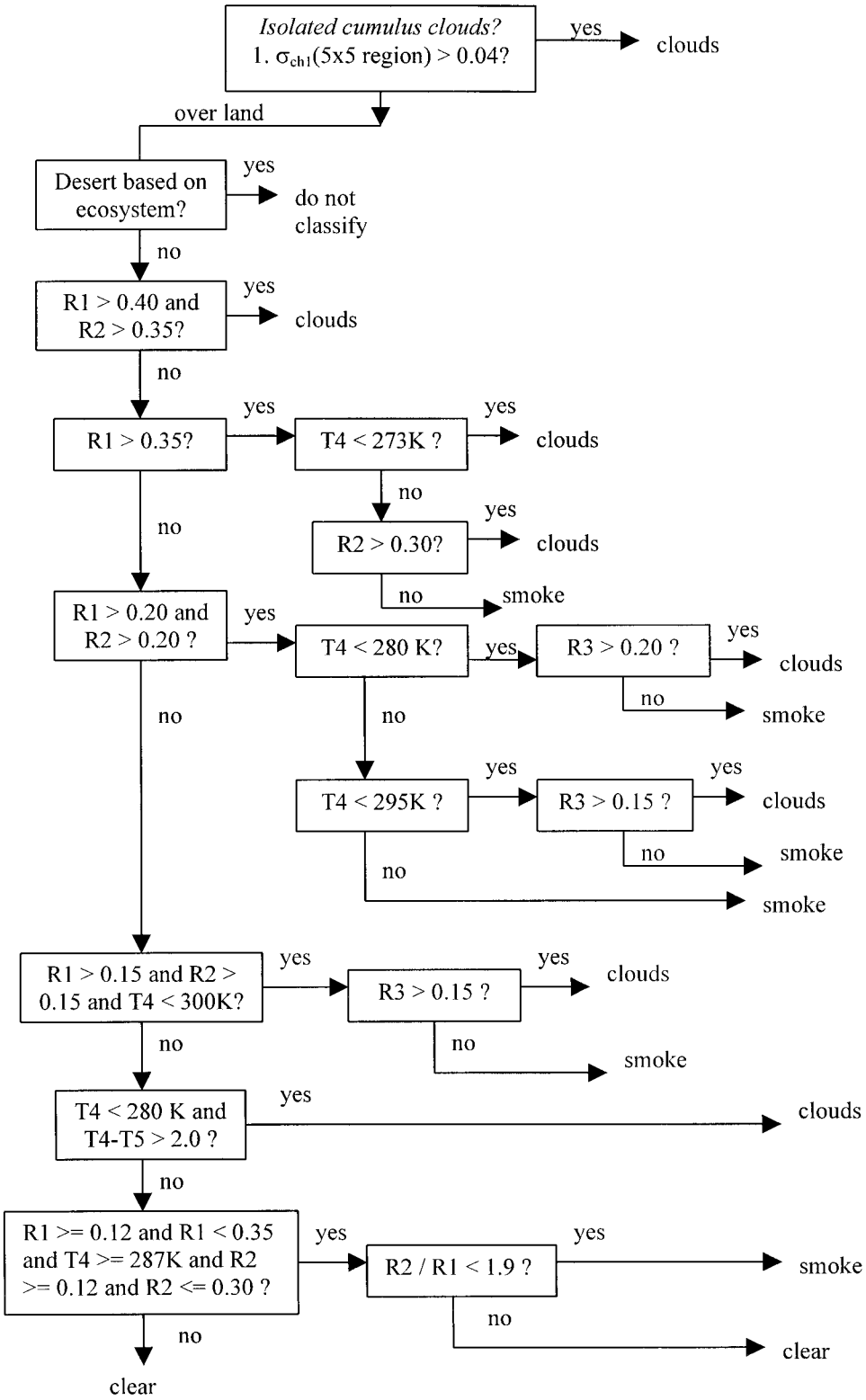

FIG. 6. Flow chart for smoke, cloud, and clear-sky pixel identification from VIRS images over land in South America.

TABLE 2. The mean broadband TOA clear-sky albedo, the statistics for the retrieved τ, estimated smoke TOA SWARF using smoke ADMs and ERBE ADMs, and TOA SWARF per optical thickness, and the number of samples for the statistics for the six surface IGBP types. Here μ represents mean value and σ represents standard deviation. Flux unit: W m^{-2}.

Surface types	Mean α_{TOA}	No. of sample	τ (0.64 μm)		Model SWARF[b]		CERES SWARF[c]		SWARF/τ	
			μ	σ	μ	σ	μ	σ	Model	CERES
Forest	0.145	6211	1.51	0.64	−54.1	23.0	−49.5	22.7	−35.8	−32.8
[a]M Forest	0.159	476	0.98	0.56	−35.5	23.3	−41.1	19.8	−36.2	−41.9
Savanna	0.144	7234	1.36	0.70	−40.5	24.2	−38.4	20.7	−29.8	−28.2
Grassland	0.144	3454	0.75	0.46	−32.5	28.7	−34.3	26.0	−43.3	−45.7
Wetland	0.149	1125	0.90	0.34	−46.6	24.5	−47.9	27.8	−51.8	−53.2
Cropland	0.159	365	0.62	0.32	−35.1	23.9	−44.3	23.6	−56.6	−71.5

[a] M Forest stands for mixed forest in the IGBP surface map.
[b] Model SWARF means the TOA SWARF calculated using smoke ADMs.
[c] CERES SWARF means the TOA SWARF calculated using CERES ERBE-like data product.

is a clear-sky sample. The broadband TOA clear-sky albedo for a grid is determined to be the minimum value of broadband TOA albedos for all clear-sky samples in August that fall into this grid. The broadband TOA albedo for a sample is determined as the ratio of CERES ES-8 ERBE-like SW flux to the downward broadband SW flux at this solar zenith angle. Second, if there are no clear-sky samples available for a grid, the minimum value out of the four neighboring grid points is used. Third, if the clear-sky albedos are not available from the four neighboring grids, the TOA clear-sky albedo for the grid is assigned as a value based on the IGBP surface type. The mean clear-sky albedo for each of the IGBP surface types is calculated from all clear-sky samples detected in August 1998. The broadband TOA clear-sky albedos for the six surface types of forest, savanna, grassland, wetland, mixed forest, and cropland are shown in Table 2.

For each of the collocated samples, the smoke, cloud, and clear-sky percentages are calculated. A sample is labeled as a smoke sample if the smoke percentage is over 90% within the CERES footprint, and the smoke τ value is retrieved using the mean value of VIRS channel-1 reflectance for this footprint. A total of 23 783 collocated data samples are labeled as smoke samples from the 14 VIRS images investigated, and 20 156 of the samples are retrieved with τ values between 0.1 to 3.5, which is the range of the lookup table. For the total of 23 783 smoke samples, over 58% of the samples are identified as clear over land in the CERES ES-8 ERBE-like data product and over 39% are identified as partly cloudy over land. Therefore, almost all smoke samples are identified as clear and partly cloudy, and the corresponding ERBE ADMs are used to convert the measured radiance into TOA fluxes in the CERES ES-8 ERBE-like product.

For each smoke sample, the TOA SW flux is estimated using the smoke ADM. Figure 7 shows the scatterplot of the SW fluxes converted using the smoke ADM versus the ES-8 ERBE-like SW fluxes. The correlation is over 96%. The mean difference between the model-estimated fluxes and the ERBE-like fluxes is 0.48 W m^{-2} with a standard deviation of 12.7 W m^{-2}. The rms error is 12.7 W m^{-2}. The relative mean difference is 15%. Therefore, based on the 14 VIRS data files, there is almost no bias between the model-estimated TOA SW fluxes and the ERBE-like SW fluxes. This result suggests that, on the average, the ERBE ADMs work well in the conversion from measured radiances to TOA SW fluxes.

For all the smoke samples, values of instantaneous smoke SWARF are calculated and grouped, based upon the IGBP surface types. The SWARF of smoke aerosols is defined as follows:

$$\text{SWARF} = F^{\uparrow}_{\text{SW,clear}} - F^{\uparrow}_{\text{SW,smoke}}, \tag{2}$$

where $F^{\uparrow}_{\text{SW,clear}}$ and $F^{\uparrow}_{\text{SW,smoke}}$ are the TOA upward SW fluxes for clear-sky conditions and smoke conditions, respectively.

Table 2 shows the instantaneous smoke TOA SWARFs for the major surface types over the area of study. The TOA SWARF values estimated from the SW fluxes converted from the ERBE ADMs and smoke ADMs for each surface type are given. The mean and standard values of retrieved τ and the TOA SWARF per unit optical thickness are also given in Table 2. For the forest surface type, the mean value of the TOA SWARF using the smoke ADMs is about 5 W m^{-2} larger that than that using the ERBE ADMs. The relative difference is about 9%. For the grassland surface type, the mean value of the TOA SWARF using the smoke ADMs is about 2 W m^{-2} smaller that that using the ERBE ADMs. The relative difference is about 6%. For the cropland surface type, the mean value of the TOA SWARF using the smoke ADMs is about 9 W m^{-2} smaller than that using the ERBE ADMs. The relative difference is over 20%. The TOA SWARFs over the six surface types range from −32 to −55 W m^{-2}, indicating that smoke aerosols have a cooling effect. These results are in good agreement with the ones from previous studies (Christopher et al. 1996, 1998). The ratios of TOA SWARFs per τ range from −28 to −71 W m^{-2}. In general, the differences of smoke TOA SWARF values estimated between using the smoke ADM and using the

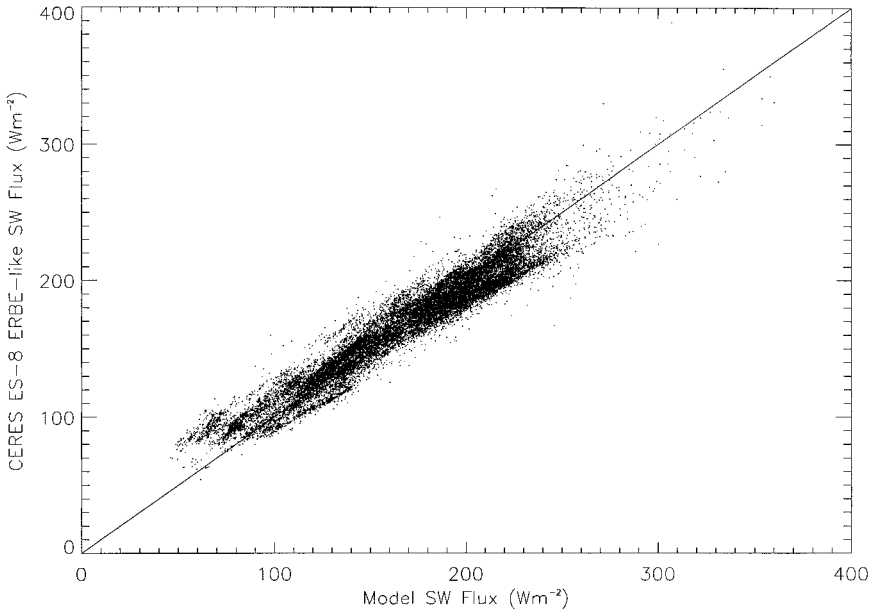

FIG. 7. Scatterplot of TOA SW fluxes converted using smoke ADMs and CERES ES-8 ERBE-like SW fluxes.

ERBE ADMs are within 10 W m^{-2}. The relative differences are within 10%.

5. Conclusions

Based on measurements made during the SCAR-B experiment, a new ADM is developed for smoke aerosols from a radiative transfer model. The ADM, a key element in the CERES program, is used to convert the observed TOA radiances to broadband fluxes. The calculated smoke ADMs are a function of aerosol τ and ω_0 values, surface albedo, solar zenith angle, satellite zenith angle, and the relative azimuth angle between sun and satellite. Comparisons of smoke ADMs with the ERBE ADMs show that although the range of the ADM values is similar between the two kinds of ADM models, the fine structures are different. The ERBE ADMs are more azimuth-angle sensitive when compared with the smoke ADMs. The relative difference of the ADM value between the two kinds of models is about 10% on average. The smoke ADM is not sensitive to the aerosol τ and ω_0 values or to the surface albedo. The uncertainty of the smoke ADM value because of uncertainties in these parameters is generally within 10%.

Using the collocated Level-1B VIRS data product and the CERES ES-8 ERBE-like data product for August 1998, TOA SW radiative forcing of biomass-burning aerosols is estimated. A threshold technique is first developed to identify smoke, cloud, and clear-sky pixels over land using VIRS channels 1, 2, 3R, 4, and 5. The threshold technique works well and identifies most of the smoke haze from the 14 VIRS images used in this study. The optical thicknesses of smoke aerosols are retrieved from VIRS channel-1 imagery using a table lookup approach. Based on the retrieved aerosol optical thickness, the ADM values for the collocated samples are determined from the precalculated lookup table, which is a function of aerosol optical thickness, single-scattering albedo, surface albedo, solar zenith angle, satellite zenith angle, and relative zenith angle. The TOA SW fluxes are then obtained by converting from the observed SW radiances using the smoke ADM values for the collocated samples.

Comparisons are made between the CERES ES-8 ERBE-like TOA SW fluxes and the TOA SW fluxes converted from the observed TOA radiances using smoke ADM. The correlation between the two datasets is about 96%. The mean difference between the CERES TOA fluxes and model-estimated fluxes is 0.48 W m^{-2}. The rms error between the two datasets is 12.7 W m^{-2}.

The TOA SWARF values for smoke aerosols are estimated based on the surface types. The TOA SWARFs range from -32 to -55 W m^{-2}, indicating that smoke aerosols have a cooling effect. The ratios of TOA SWARFs per unit optical thickness range from -29 to -57 W m^{-2}. The differences of estimated TOA SWARFs using CERES SW fluxes and SW fluxes from smoke ADMs are within 10 W m^{-2}. The relative differences are generally less than 10%.

Acknowledgments. This research is partially supported by NASA Grants NAS1-98131 as part of the CERES project, and NAGW-5195, NAG5-8404, and NCC8141 as part of the Global Aerosol Climatology Project. Xiang Li is supported under NASA's Earth System Science Fel-

lowship program (NASA reference number ESS/98-0000-0115). The CERES data were obtained from the NASA Earth Observing System Data and Information System, Distributed Active Archive Center (DAAC) at the Langley Research Center and the VIRS data were obtained through the NASA Goddard Space Flight Center DAAC. We also thank Drs. Ricchiazzi and Gautier for making the SBDART code available. Appreciation is also extended to Drs. Tsay and Arnold for providing the BRDF data for cerrado and forest surfaces.

REFERENCES

Ackerman, T. P., and O. B. Toon, 1981: Absorption of visible radiation in atmosphere containing mixtures of absorbing and nonabsorbing particles. *Appl. Opt.,* **20,** 3661–3667.

Andreae, M. O., 1991: Biomass burning: Its history, use, and distribution and its impact on environmental quality and global climate. *Global Biomass Burning,* J. S. Levine, Ed., The MIT Press, 569 pp.

Barkstrom, B. R., 1984: The Earth Radiation Budget Experiment. *Bull. Amer. Meteor. Soc.,* **65,** 1170–1185.

Christopher, S. A., D. V. Vulcan, J. Chou, and R. M. Welch, 1996: First estimates of the radiative forcing of aerosols from biomass burning from satellite data. *J. Geophys. Res.,* **101,** 21 256–21 273.

——, M. Wang, T. A. Berendes, R. M. Welch, and S. K. Yang, 1998: The 1985 biomass burning season in South America: Satellite remote sensing of fires, smoke, and regional radiative energy budget. *J. Appl. Meteor.,* **37,** 661–678.

——, J. Chou, J. Zhang, X. Li, and R. M. Welch, 2000: Shortwave direct radiative forcing of biomass burning aerosols estimated from VIRS and CERES. *Geophys. Res. Lett.,* in press.

Crutzen, P. J., L. E. Heidt, J. P. Kransec, W. H. Pollack, and W. Seiler, 1979: Biomass burning as a source of atmospheric gases CO, H_2, N_2, CH_3Cl, and COS. *Nature,* **282,** 253–256.

Green, R. N., 1987: Earth Radiation Budget Experiment (ERBE) Data Management System Processed Archival Tape S-8 PAT users's guide. NASA Langley Research Center, 46 pp. [Available online at http://charm.larc.nasa.gov/GUIDE/dataset_documents/erbe_58.html#7.]

——, and B. A. Wielicki, 1995: Clouds and the Earth's Radiant Energy System (CERES) algorithm theoretical basis document, subsystem 4.4. Vol. III, NASA Reference Publ. 1376, 259 pp.

——, ——, J. A. Coakley III, L. L. Stowe, and P. O'R. Hinton, 1995: Clouds and the Earth's Radiant Energy System (CERES) algorithm theoretical basis document, subsystem 4.5. Vol. III, NASA Reference Publ. 1376, 259 pp.

Hao, W. M., and M.-H. Liu, 1994: Spatial and temporal distribution of biomass burning. *Global Biogeochem. Cycl.,* **8,** 495–503.

Hobbs, P. V., J. S. Reid, R. A. Kotchenruther, R. J. Ferek, and R. Weiss, 1997: Direct radiative forcing by smoke from biomass burning, *Science,* **275,** 1776–1778.

Houghton, J. T., L. G. Meira Filho, B. A. Callander, N. Harris, A. Kattenberg, and K. Maskell, Eds., 1996: *Climate Change 1995: The Science of Climate Change.* Cambridge University Press, 572 pp.

Kaufman, Y. J., and T. Nakajima, 1993: Effect of Amazon smoke on cloud microphysics and albedo—analysis from satellite imagery. *J. Appl. Meteor.,* **32,** 729–744.

——, and Coauthors, 1998: The Smoke, Cloud and Radiation Experiment in Brazil (SCAR-B). *J. Geophys. Res.,* **103,** 31 783–31 808.

Keiffer, H. H., and R. L. Wildey, 1996: Establishing the moon as a spectral radiance standard. *J. Atmos. Oceanic Technol.,* **13,** 360–375.

Kummerow, C., W. Barnes, T. Kozu, J. Shuie, and J. Simpson, 1998: The Tropical Rainfall Measuring Mission (TRMM) sensor package. *J. Atmos. Oceanic Technol.,* **15,** 809–817.

Li, X., S. A. Christopher, J. Zhang, J. Chou, and R. M. Welch, 1999: Aerosol single scattering albedo estimated from *NOAA-14* AVHRR measurements: Case studies over Brazil. *Proc. SPIE,* **3756,** 374–383.

Li, Z., H. G. Leighton, K. Masuda, and T. Takashima, 1993: Estimation of SW flux absorbed at the surface from TOA reflected flux. *J. Climate.,* **6,** 317–330.

Loveland, T., and A. S. Belward, 1997: The IGBP-DIS global 1-km land cover data set: First results. *Int. J. Remote Sens.,* **18,** 3289–3295.

Lubin, D., and P. G. Weber, 1995: The use of cloud reflectance functions with satellite data for surface radiation budget estimation. *J. Appl. Meteor.,* **34,** 1333–1347.

Martins, J. V., P. Artaxo, C. Liousse, J. S. Reid, P. V. Hobbs, and Y. J. Kaufman, 1998: Effects of black carbon content, particle size, and mixing on light absorption by aerosols from biomass burning in Brazil. *J. Geophys. Res.,* **103,** 32 041–32 050.

McClatchey, R. A., R. W. Fenn, J. E. A. Selby, F. E. Volz, and J. S. Garing, 1972: Optical properties of the atmosphere. Environmental Research Paper AFCRL-72-0497, 108 pp. [Available from Air Force Cambridge Research Laboratory, Bedford, MA 01730.]

Penner, J. E., R. E. Dickinson, and C. A. O'Neill, 1992: Effects of aerosols from biomass burning on the global radiation budget. *Science,* **256,** 1432–1433.

Pierluissi, J. H., and G.-S. Peng, 1985: New molecular transmission band models for LOWTRAN. *Opt. Eng.* **24,** 541–547.

Reid, J. S., P. V. Hobbs, R. J. Ferek, D. R. Blake, J. V. Martins, M. R. Dunlap, and C. Liousse, 1998: Physical, chemical, and optical properties of regional hazes dominated by smoke in Brazil. *J. Geophys. Res.,* **103,** 32 059–32 080.

Remer, L. A., Y. J. Kaufman, B. N. Holben, A. M. Thompson, and D. McNamara, 1998: Biomass burning aerosol size distribution and modeled optical properties. *J. Geophys. Res.,* **103,** 31 879–31 891.

Ricchiazzi, P., S. Yang, C. Gautier, and D. Sowle, 1998: SBDART: A research and teaching software tool for plane-parallel radiative transfer in the earth's atmosphere. *Bull. Amer. Meteor. Soc.,* **79,** 2101–2114.

Ross, J. L., P. V. Hobbs, and B. Holben, 1998: Radiative characteristics of regional hazes dominated by smoke from biomass burning in Brazil: Closure tests and direct radiative forcing. *J. Geophys. Res.,* **103,** 31 925–31 941.

Sailer, W., and P. J. Crutzen, 1980: Estimates of gross and net fluxes of carbon between the biosphere and atmosphere from biomass burning. *Climatic Change,* **2,** 207–247.

Stamnes, K., S. Tsay, W. Wiscombe, and K. Jayaweera, 1988: Numerically stable algorithm for discrete-ordinate-method radiative transfer in multiple scattering and emitting layered media. *Appl. Opt.,* **27,** 2502–2509.

Suttles, J. T., and Coauthors, 1988: Angular radiation models for earth–atmosphere system. I—Shortwave radiation. NASA RP-1184, 144 pp.

——, ——, G. L. Smith, B. A. Wielicki, I. J. Walker, V. R. Taylor, and L. L. Stowe, 1989: Angular radiation models for earth–atmosphere system. II—Longwave radiation. NASA RP-1184, 144 pp.

——, B. A. Wielicki, and V. Sastri, 1992: Top-of-atmosphere radiative fluxes—validation of ERBE scanner inversion algorithm using *Nimbus-7* ERB data. *J. Appl. Meteor.,* **31,** 784–796.

Tsay, S.-C., M. D. King, G. T. Arnold, and J. Y. Li, 1998: Airborne spectral measurements of surface anisotropy during SCAR-B. *J. Geophys. Res.,* **103,** 31 943–31 953.

Wielicki, B. A., R. N. Green, C. J. Tolson, and A. Fan, 1995: Clouds and the Earth's Radiant Energy System (CERES) Algorithm Theoretical Basis Document, Subsystem 4.0. Vol. III, NASA RP-1376, 259 pp.

——, B. R. Barkstrom, E. F. Harrison, R. B. Lee III, G. L. Smith, and J. E. Cooper, 1996: Clouds and the Earth's Radiant Energy System (CERES): An Earth Observing System experiment. *Bull. Amer. Meteor. Soc.,* **77,** 853–868.

Wiscombe, W. J., and J. W. Evans, 1977: Exponential-sum fitting of radiative transmission functions. *J. Comput. Phys.,* **24,** 416–444.